coatings

MDPI

Article

Component Engineering of Multiphase Nickel Sulfide-Based Bifunctional Electrocatalysts for Efficient Overall Water Splitting

Nianrui Qu [1], Lu Han [1], Tianhui Wu [1,*], Qingzhi Luo [2], Shoufeng Tang [1,*], Jianmin Gu [1] and Desong Wang [1,2,*]

[1] State Key Laboratory of Metastable Materials Science and Technology (MMST), Hebei Key Laboratory of Applied Chemistry, Yanshan University, Qinhuangdao 066004, China; qunianrui@ysu.edu.cn (N.Q.); hlhm19980515@163.com (L.H.); jmgu@ysu.edu.cn (J.G.)

[2] School of Sciences, Hebei University of Science and Technology, Shijiazhuang 050018, China; lqz2004-1@163.com

* Correspondence: wth@ysu.edu.cn (T.W.); tangshf@ysu.edu.cn (S.T.); dswang06@126.com (D.W.)

Abstract: The development of highly efficient and low-cost bifunctional electrocatalysts for water splitting has become increasingly attractive. So far, the strategies to optimize electrocatalytic performance have mainly focused on enhancing the active sites and regulating the surface structures through doping foreign metal or anions into the composites; however, the internal and external adjustments achieved by tuning the chemical composition and crystalline phases in a material in order to investigate the composition-dependent catalytic activity has generally remained limited. Here, through various in situ composition-dependent nickel sulfides grown while controlling the sulfidation degree, we achieve the precise regulation of nickel sulfides from a single-phase component to multiple-phase components (i.e., two-phase components and three-phase components), further comparing the hydrogen evolution reaction (HER) and oxygen evolution reaction (OER) performances. Benefiting from the synergy of an analogous uniform nanoarray structure and excellent intrinsic activation, the as-obtained Ni_xS_y-5, with three-phase components, shows low overpotentials at 10 mA cm^{-2} for HER (148 mV) and OER (111 mV), as well as a low cell voltage of 1.48 V for overall water splitting in alkaline media, which are among the best results ever reported for overall water splitting.

Keywords: nickel sulfide; component engineering; bifunctional electrocatalyst; overall water splitting

check for updates

Citation: Qu, N.; Han, L.; Wu, T.; Luo, Q.; Tang, S.; Gu, J.; Wang, D. Component Engineering of Multiphase Nickel Sulfide-Based Bifunctional Electrocatalysts for Efficient Overall Water Splitting. *Coatings* **2023**, *13*, 1938. https://doi.org/10.3390/coatings13111938

Academic Editor: Aivaras Kareiva

Received: 16 October 2023
Revised: 7 November 2023
Accepted: 11 November 2023
Published: 14 November 2023

1. Introduction

Electrochemical water splitting is recognized as a sustainable technology for the production of clean and green hydrogen, which provides a promising pathway to achieve the goal of carbon neutralization [1–4]. The overall water splitting process involves two half-reactions: the hydrogen evolution reaction (HER) and the oxygen evolution reaction (OER) [5,6]. The efficiency of the process depends on the overpotentials that must be used for overcoming the energy barriers inherent in the two half-reactions [7–9]. Heretofore, the major obstacles restricting commercialized applications of water-splitting devices were the lack of highly efficient electrocatalysts with low overpotential requirements for both the HER and OER processes [10–14]. It remains difficult to develop two such electrocatalysts that could be coupled in an integrated electrolyzer for overall water splitting, as their optimal operating modes often mismatch [15,16]. Coupling two catalysts in two different conditions that can make them work best and integrating them into a single water separation device is more complicated, due to the requirements of different accessories, preparations, and optimization procedures [17–20]. Thus, it is urgent to design efficient bifunctional electrocatalysts in the same electrolyte that can work well for both HER and OER.

The platinum (Pt)-group materials have shown highly efficient electrocatalytic performance, but high cost and elemental scarcity significantly hinder their widespread

application [21–24]. Recently, first-row transition metal-based catalysts, such as metal oxides [25,26], sulfides [27,28], selenides [29], phosphides [30–33], and hydroxides [34] of Co, Ni, and Fe, have been intensively investigated due to their high intrinsic activities and low cost. Among these, nickel sulfides with diverse crystalline phases (i.e., nickel subsulfide (Ni_3S_2), nickel sulfide (NiS), and nickel disulfide (NiS_2), etc.) have been considered as promising water-splitting electrocatalysts because of their good conductivity and unique 3D configuration [35–38]. Although nickel sulfide-based electrocatalysts with different crystal structures have all been separately studied as HER/OER catalysts, the further enhancement of the electrocatalytic activity of these materials is still greatly limited due to their low surface active exposure and poor long-term stability. Doping foreign high-active transition metal into nickel sulfide-based catalysts is regarded as an efficient route to optimize their electrochemical performance by overcoming the intrinsic activation barriers [39–41]; however, the doping strategy usually shows a tendency to include the various metal-active sites, leading to a significant impact on the study of intrinsic catalytic activity [42,43]. In principle, the catalytic property of a material is determined using its electronic structure and can be regulated by engineering its composition and morphology [44–46]. The internal and external adjustments, i.e., tuning the electronic structure through phase control and composition adjustment, are valid for the production of efficient electrocatalysts [47–49]. Guided by the above design ideas, nickel sulfides with various crystalline phases (such as Ni_3S_2, NiS, and NiS_2, etc.) were used as ideal models for tuning the chemical composition and crystalline phases in a material, offering a good opportunity to investigate the composition-dependent catalytic activity by constructing the composition–structure–performance relationship for designing high-performance catalysts.

Herein, we present a facile design of various in situ grown composition-dependent nickel sulfides by precisely controlling the sulfidation degree in a simple hydrothermal process, achieving the regulation of nickel sulfides from a single-phase component to multiple-phase components (i.e., two-phase components and three-phase components), with the amount of thiourea gradually increased from 2 mmol to 7 mmol, thus intrinsically comparing the HER and OER performance in various-phase nickel sulfide-based systems. Specifically, benefiting from the higher exposed active surface, the increased charge transfer capacity, and the lower charge-transfer resistance, the vertically aligned Ni_xS_y-5 nanoarrays, with three-phase components, exhibit exceptional bifunctional electrocatalytic performance towards both OER and HER under alkaline media. Notably, Ni_xS_y-5 shows remarkable HER and OER activities, with overpotentials of 148 mV and 111 mV to deliver the current density of 10 mA cm^{-2}, respectively, which is superior to the performance of the majority of non-noble metal electrocatalysts under alkaline conditions. Furthermore, utilizing the Ni_xS_y-5 nanoarrays as bifunctional electrocatalysts, an alkaline electrolyzer at 10 mA cm^{-2} is operated at a low cell voltage of 1.48 V, significantly lower than that of state-of-the-art overall-water-splitting electrocatalysts (cell voltages > 1.6 V).

2. Experimental

Chemicals

Otassium hydroxide (KOH, 96.0%) and thiourea (CH_4N_2S, 99.0%) were purchased from Tianjin Kermel Chemical Reagent Co., Ltd. (Tianjin, China) Hydrochloric acid (HCl, 37%), acetone (C_3H_6O, 99.9%), and ethyl alcohol (CH_3CH_2OH, 99.7%) were purchased from Qinhuangdao Chemical Co., Ltd. (Qinhuangdao, China) Nickel foam (NF) was purchased from Shenzhen Green and Creative Environmental Science and Technology Co., Ltd. (Shenzhen, China) All the reagents were employed directly, without further refinement. The water used throughout all the experiments was purified using a Millipore system. Pieces of nickel foam, used as a substrate, were washed by sonication consecutively with 3 M HCl, acetone, and deionized water.

Synthesis of multiple-component Ni_xS_y composites

Typically, the different amounts of thiourea (2–3–4–5–6–7 mmol) were dissolved in 10 mL of water under continuous magnetic stirring for about 20 min to obtain different concentrations of aqueous solutions. Then, the acidified surface-cleaned Ni foam (Figure S1), as an Ni source, was immersed in the above solution, and the mixture was subsequently placed into a 23 mL autoclave with a Teflon liner at 180 °C for 16 h. When the mixture cooled down to 30 °C, the reaction mixture were separated from the solution and cleaned three times with deionized water to remove the unreacted impurities. Finally, the corresponding nickel sulfide products with different phase components, denoted as Ni_xS_y-2, Ni_xS_y-3, Ni_xS_y-4, Ni_xS_y-5, Ni_xS_y-6, and Ni_xS_y-7, respectively, were obtained by drying at 75 °C overnight in a vacuum oven.

Characterization

These samples were assessed by scanning electron microscopy (SEM, SUPRA 55, Carl Zeiss AG, Jena, Germany), X-ray diffraction (XRD, Bruker AXSD8 diffractometer, BRUKER AXS GMBH, Karlsruhe, Germany), and X-ray photoelectron spectroscopy (XPS, ESCALAB 250Xi, Thermo Fisher Scientific, Waltham, MA, USA). The acquired XPS data were refined via standard carbon peaks.

Electrochemical measurements

The CHI 660E device, with a three-electrode system, was employed to record the electrocatalytic activity of these catalysts in 1 M KOH aqueous solution. The three-electrode system comprised a working electrode (the samples) with a dimension of 1 cm × 2 cm, a reference electrode (Hg/HgO), and a counter electrode (a graphite rod). The potentials were determined using the Hg/HgO electrode, and they can be transformed into RHE based on the equation ERHE = $E_{Hg/HgO}$ + 0.0591 pH + 0.0977. For measuring the electrocatalytic activities of these samples in HER and OER, the polarization curves were acquired using linear scanning voltammetry (LSV), with scan rate of 5 mV. Electrochemical impedance spectroscopy (EIS) measurements were carried out in a frequency range of 0.01 Hz~1 MHz. Double-layer capacitance (C_{dl}) was assessed via cyclic voltammetry (CV), with diverse scan rates of 10–50 mV s^{-1}.

3. Results and Discussion

In the typical synthetic strategy, the acidified Ni foam was used as a surplus Ni source and a support material, and the different amounts of thiourea (2 mmol, 3 mmol, 4 mmol, 5 mmol, 6 mmol, and 7 mmol) played the significant role of chemical etching for the direct sulfidation of NF in a hydrothermal process, offering a good opportunity to allow the in situ formation of nickel sulfides of different sulfidation degrees and different crystalline phases. The compositions of the synthesized samples were detected using standard XRD measurements (Figure 1a). The diffraction peaks of Ni_xS_y-2 and Ni_xS_y-3 are in good agreement with the orthorhombic phases of Ni_3S_2 (JCPDS: 44-1418), except for the observed pronounced diffraction peaks of the Ni substrate (51.8°), which suggest the formation of Ni_3S_2 in Ni_xS_y-2 and Ni_xS_y-3. As the thiourea content increased to 4 mmol, all the diffraction peaks of Ni_xS_y-4 became well indexed to hexagonal Ni_3S_2 (JCPDS: 44-1418) and Ni_7S_6 (PDF: 14-0364), without additional diffraction peaks of other impurities, in which corresponding diffraction peaks of Ni foam all disappeared, confirming the high purity of Ni_xS_y-4. Notably, there were three crystalline phases in the Ni_xS_y-5 structure, where, in addition to Ni_3S_2 and Ni_7S_6 mentioned above, a new phase NiS appeared (JCPDS: 12-0041). When the content of thiourea was further increased to 6 mmol and 7 mmol, all the diffraction peaks of Ni_3S_2 disappeared, and both Ni_xS_y-6 and Ni_xS_y-7 contained only two phases of nickel sulfides (i.e., Ni_7S_6 and NiS). These results indicate that changing the thiourea content can achieve the manipulation of nickel sulfides from a single-phase component to multiple-phase components (i.e., two-phase components and three-phase components), making various composition-dependent nickel sulfides good platforms for evaluating the composition–structure–performance relationships.

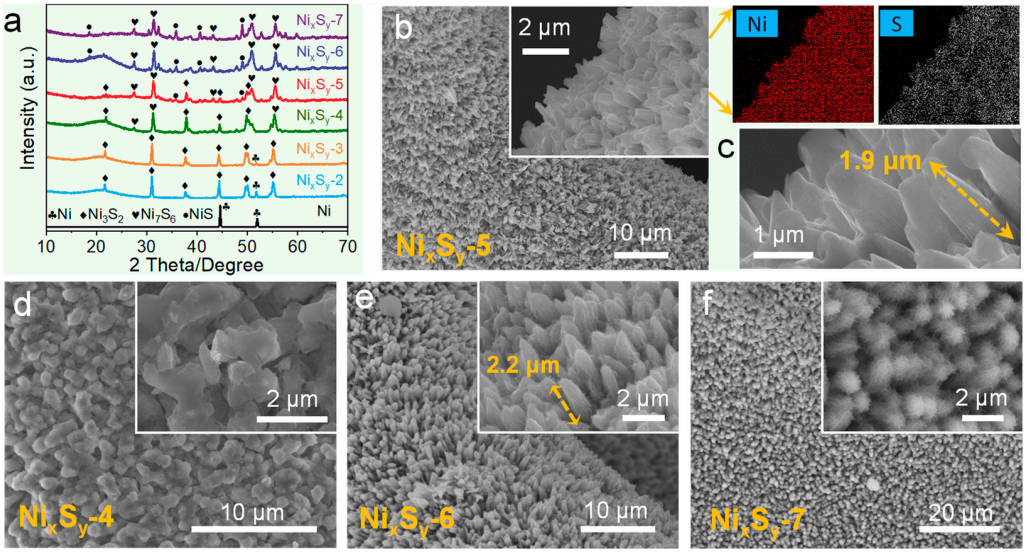

Figure 1. (**a**) XRD patterns of all the as-prepared samples of the nickel sulfides. SEM images of Ni_xS_y-5 (**b**,**c**), Ni_xS_y-4 (**d**), Ni_xS_y-6 (**e**), and Ni_xS_y-7 (**f**). The insets exhibit the corresponding high magnification SEM image, respectively.

The morphologies of all the samples were revealed using SEM, indicating that the as-obtained samples formed in different sulfidation processes elucidate the manner in which varying the sulfidation degree led to the diverse morphologies of the samples (Figures 1 and S2). Generally, Ni_xS_y-2, Ni_xS_y-3, and Ni_xS_y-4 present irregular morphologies, while the Ni_xS_y-5, Ni_xS_y-6, and Ni_xS_y-7 show analogous uniform rod-like arrays, homogeneously distributed across the entire NF surface. Notably, in Ni_xS_y-2, compared to other sulfidation conditions, Ni_3S_2 grew on the surface of the nickel foam, without any aggregation, but this growth was not sufficient to completely cover the NF surface due to the low-degree sulfidation (Figure S2a). With further increase in the degree of sulfidation, it can be found that the whole Ni surface is densely covered with irregular morphology in Ni_xS_y-3 and Ni_xS_y-4 (Figures S2b and 1d). Different from Ni_xS_y-2, Ni_xS_y-3, and Ni_xS_y-4, the rod-like nanoarrays are grown across the NF surface for Ni_xS_y-5, Ni_xS_y-6, and Ni_xS_y-7. Notably, Ni_xS_y-5 nanoarrays, with uniformly distributed Ni and S elements across the structure, grow almost uniformly and vertically on the NF surface, with an average length of about 1.9 μm, indicating an evident anisotropic growth behavior (Figure 1b,c), which may result in more active sites. Compared to Ni_xS_y-5, Ni_xS_y-6 nanoarrays with a higher degree of sulfidation, have a longer length of about 2.2 μm, arranged with clear crossover between the rod-like structures (Figure 1e), and the degree of crossover increases as the sulfidation further enhances, as observed in Ni_xS_y-7 (Figure 1f).

The XPS analyses are carried out to determine the predominant constituent elements and characterize the corresponding chemical valence states. All observed peaks are assigned to the expected elements, including Ni, S, O, and adventitious C (Figure S3). Notably, the spectrum of Ni_xS_y-2 does not show peaks of the S elements, which is attributed to the low-degree sulfidation due to the small amount of S content, which is difficult to effectively detect; the signal of the S 2*p* peak gradually increases with the further improvement of the sulfidation degree. The Ni 2*p*, S 2*p*, and O 2*p* fitting spectra of all the samples are displayed in Figures S4–S6, respectively, as obtained by the Gaussian fitting. For the Ni 2*p* region, the high-resolution XPS spectrum displays two main peaks at 855.9 and 873.4 eV, ascribed to Ni $2p_{3/2}$ and Ni $2p_{1/2}$, respectively, as well as typical shakeup satellite peaks located at 880.3 and 861.6 eV (Figure S4) [50]. For the S 2*p* spectrum, the peaks in all samples, assigned to the S $2p_{1/2}$ and $2p_{3/2}$ orbitals of the divalent sulfide ions (S^{2-}), are observed at 163.8 and 162.6 eV, [51,52], in addition to the SO_4^{2-} peaks above 168.7 eV (originating from the surface oxidation). With the further improvement of the sulfidation degree, in addition to the three XPS peaks mentioned above, additional sets of peaks appear in the spectrum. The

binding energies of S $2p_{1/2}$ and $2p_{3/2}$ at 164.4 and 165.6 eV show the existence of bridging S_2^{2-} (Figure S5) [51,53]. Although it is impossible to exclusively evaluate the ratio between the two types of sulfur species of S^{2-} and S_2^{2-} because of their similar binding energies, the existence of the higher energy peaks in Ni_xS_y-5, Ni_xS_y-6, and Ni_xS_y-7 are likely related to the high electrochemical water splitting activity. The O 1s spectra of all the samples were determined to identify the oxides generated on the surface. Notably, the O 1s spectra of all the samples are classified into two categories (denoted as O1 and O2) [54]. The O2 peak of oxygen vacancy is located at ≈531.2 eV, and the peak of O1 at ≈532.5 eV is related to the hydroxy species of the adsorbed water molecules [55] (Figure S6).

Accordingly, only a representative Ni_xS_y-5 with three-phase components, which exhibits the existence of four elements (Ni, S, O, and C) (Figure 2a), is discussed in detail. The Ni 2*p* peaks at ≈855.7 and ≈873.1 eV for Ni_xS_y-5 are assigned to Ni^{2+} $2p_{3/2}$ and Ni^{2+} $2p_{1/2}$, respectively, and the peaks at ≈857.2 eV for Ni $2p_{3/2}$ and at ≈874.6 eV for Ni $2p_{1/2}$ manifest the existence of high-valence Ni^{3+}, with the ratio of Ni^{3+} and Ni^{2+} ≈ 0.6 (Figure 2b). Notably, the intensity of the S_2^{2-} peak in NixSy-5 is significantly higher than that in Ni_xS_y-6 and Ni_xS_y-7, producing more bridging S_2^{2-}, which is considered to possess the most active sites in Ni_xS_y-5 (Figure 2c). The area of O2 is obviously larger than that of O1 in Ni_xS_y-5, suggesting that there are more oxygen sites in the NiO produced by surface oxidation than that in the absorbed water molecules [56,57] (Figure 2d).

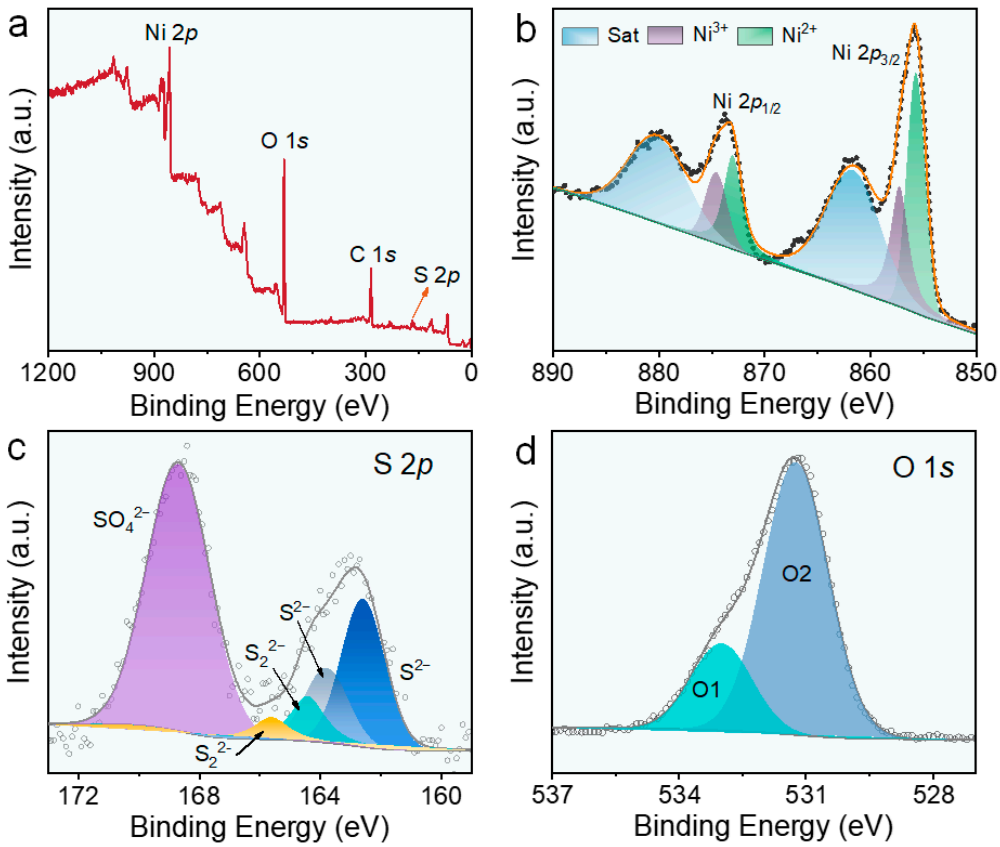

Figure 2. XPS spectra of (**a**) the survey spectrum, (**b**) the Ni 2*p* spectrum, (**c**) the S 2*p* spectrum, and (**d**) the O 1s spectrum in Ni_xS_y-5.

As Ni_xS_y-2 and Ni_xS_y-3 possess the same single-phase component of Ni_3S_2, as well as the same two-phase components of Ni_7S_6 and NiS in Ni_xS_y-6 and Ni_xS_y-7, the detailed description of the electrocatalysis performance is only illustrated for Ni_xS_y-3 and Ni_xS_y-7. The HER electrocatalysis was measured in 1 M KOH electrolyte by a three-electrode system, and Hg/HgO and a graphite rod were selected as reference and counter electrodes, respectively, offering a good opportunity to study the component-dependent catalytic activity based

on the single-phase-component Ni_xS_y-3 electrodes, the two-phase-component electrodes of Ni_xS_y-4 and Ni_xS_y-7, as well as the three-phase-component electrodes of Ni_xS_y-5. As illustrated in Figure 3a, Ni_xS_y-5 shows a remarkable HER catalytic activity at 10 mA cm^{-2}, with the lowest overpotential of 148 mV after activation by cyclic voltammetry among all the samples, which is about 69 mV higher than that of the commercial Pt/C catalyst [58]. The activity of Ni_xS_y-5 is stronger than that of Ni_xS_y-7 (169 mV), and largely exceeds that of Ni_xS_y-4 (196 mV) and Ni_xS_y-7 (216 mV). Notably, despite the presence of two-phase components in both Ni_xS_y-4 (Ni_3S_2 and Ni_7S_6) and Ni_xS_y-7 (Ni_7S_6 and NiS), there is a clear difference in the electrocatalytic properties for Ni_xS_y-4 (196 mV) and Ni_xS_y-7 (169 mV), presumably because of the presence of bridging S_2^{2-}, which is highly active in Ni_xS_y-7. To clearly identify the catalysts with the best activity, the overpotentials of all the samples are shown at 10, 20, and 50 mA cm^{-2} using a visual bar graph (Figure 3b). As the current density gradually increases, Ni_xS_y-5 still exhibits the lowest overpotential, which is probably attributable to the fact that the Ni_xS_y-5 electrodes with a three-phase structure can provide more oxygen vacancies and more active sites for the HER reaction. These results reveal that the catalytic performance of the Ni_xS_y-5 electrodes is also superior to that of the majority of non-noble metal HER electrocatalysts in alkaline media (Table S1).

The Tafel plots were acquired via fitting the linear regions of the LSV curves based on the Tafel equation, which manifested the HER kinetics of the electrocatalysts (Figure 3c). The Tafel slope of the Ni_xS_y-5 electrodes was 140 mV dec^{-1}, the lowest value among all the samples, which is smaller than that of the two-phase component electrodes (with comparable Tafel slopes of 151 and 158.1 mV dec^{-1} for Ni_xS_y-4 and Ni_xS_y-7, respectively), and much smaller than that of single-phase component Ni_xS_y-3 electrodes (171.1 mV dec^{-1}). The results show that Ni_xS_y-5 exhibits faster reaction kinetics and better charge transfer abilities in the HER electrocatalysis processes. Accordingly, these various HER activities demonstrate that the HER performance could be rationally tuned via changing the chemical composition of the nickel sulfide-based electrodes.

For gaining deep insight into the efficient HER activities of various phase-component electrodes, the SEM images have revealed that the as-prepared Ni_xS_y-5 exhibit looser and more uniform nanoarrays than those of other samples, showing that the Ni_xS_y-5 electrode can offer larger active surface areas during catalytic reactions. For confirming this result experimentally, the C_{dl} analyses are carried out for evaluating the electrochemically active surface area (ECSA). The CV curves of the as-obtained nickel sulfide electrodes in Figure S7 show that the slope of the linear plot of the non-faradaic capacitance current as a function of the scan rate is equal to C_{dl}. Notably, the Ni_xS_y-5 electrode possesses the largest C_{dl} value of 142 mF cm^{-1}, which is obviously superior to that of the single-phase component Ni_xS_y-3 electrodes (30.3 mF cm^{-1}) and that of the two-phase component electrodes of Ni_xS_y-4 (85 mF cm^{-1}) and Ni_xS_y-7 (133.5 mF cm^{-1}), suggesting that Ni_xS_y-5 possesses a larger surface area, thus possessing more exposed catalytical active sites in the HER process. The conductivity of the catalyst is another significant factor that affects the overall electrocatalytic activity [59]. Compared to other samples, the Ni_xS_y-5 electrocatalyst showed the smallest semicircle within the high-frequency range in the Nyquist curve (Figure 3e), indicating the weakest charge-transfer resistance in the catalyst/electrolyte interface and faster charge transport kinetics, in agreement with its excellent electrocatalytic activity. Moreover, the long-term stability test was conducted for studying the durability of the constructed electrolyzer using the constant voltage technique. Notably, all the samples exhibited a stable cathodic current, with almost negligible degradation (Figure 3f), which indicates good durability, showing that the samples and can maintain catalytic activities for at least several hours in the Ni_xS_y-5 electrode.

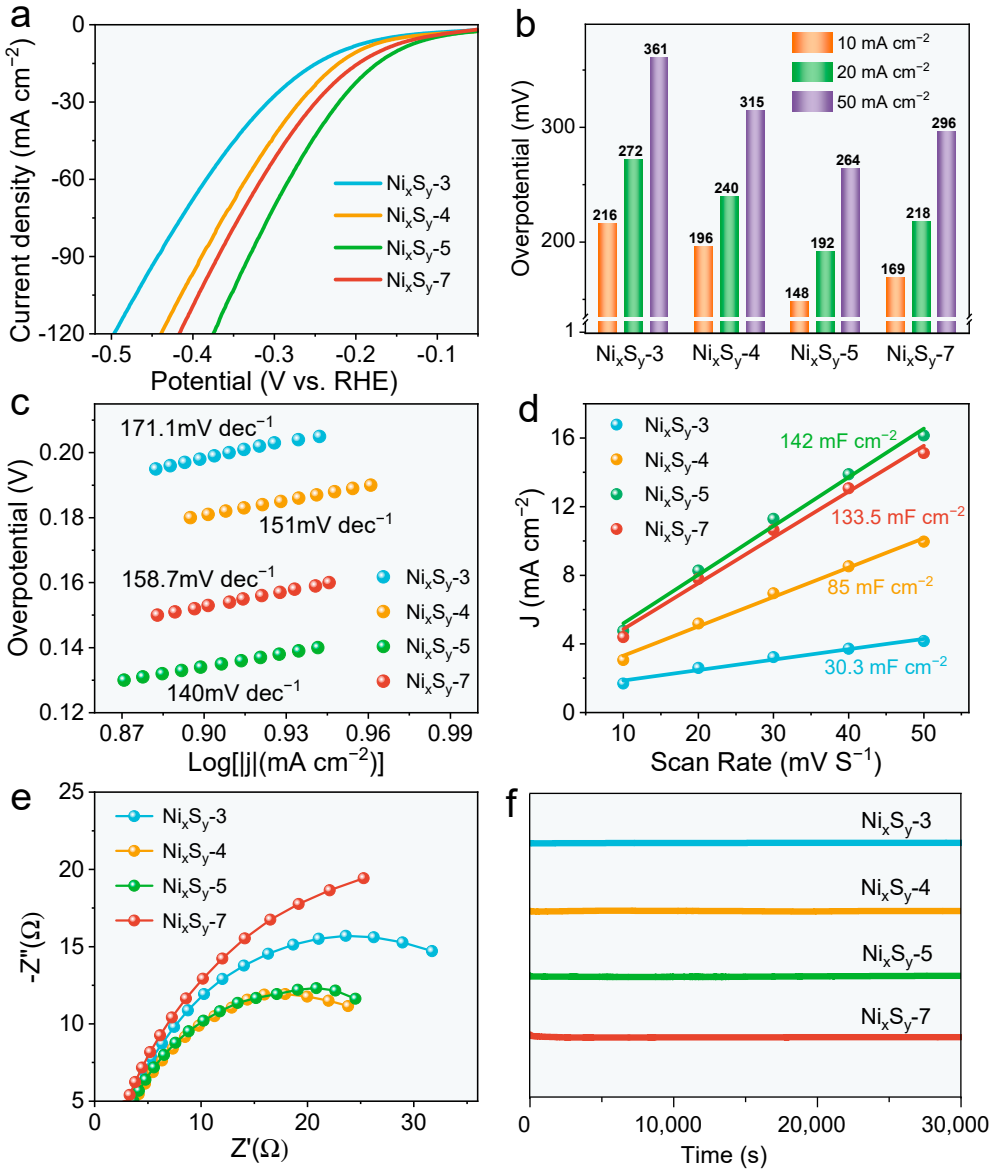

Figure 3. The HER performance data of the as-prepared electrocatalysts in 1.0 M KOH. (**a**) HER polarization curves (iR-corrected) measured with a scan rate of 5 mV s^{-1}; (**b**) comparison of overpotential of as-prepared electrodes at different current densities of 10 mA cm^{-2}, 20 mA cm^{-2}, and 50 mA cm^{-2}; (**c**) the corresponding Tafel curves; (**d**) the linear plots of the capacitive current versus the scan rate; (**e**) the corresponding EIS plot; (**f**) stability test regarding HER at a constant current density of 10 mA cm^{-2}.

To investigate the OER performance of the as-obtained electrode materials, the corresponding electrochemical analyses have been performed under alkaline conditions. As expected, Ni_xS_y-5 exhibits the best OER property among all the catalysts, with a minimum overpotential of 111 mV for driving the current density of 10 mA cm^{-2} (Figure 4a), which is much lower than that of the single-phase component Ni_xS_y-3 electrodes (229 mV) and the two-phase component electrodes of Ni_xS_y-4 (131 mV) and Ni_xS_y-7 (113 mV), which is also about 159 mV less than that of state-of-the-art RuO_2 catalyst.[7] Moreover, the overpotential values at 10, 20, 50, and 100 mA cm^{-2} are shown in the visual bar graph (Figure 5b), indicating that the OER performance of Ni_xS_y-5 is also competitive as compared to that of the recently reported non-precious electrocatalyst (Figure 4b,c and Table S2). The OER kinetics of the as-prepared electrocatalysts was assessed using a Tafel plot (Figure 4d), which delivered an impressive Tafel slope of 60 mV dec^{-1} for Ni_xS_y-5, smaller than that

of the Ni_xS_y-3 electrodes (70 mV dec^{-1}) and Ni_xS_y-4 (69.9 mV dec^{-1}), as well as Ni_xS_y-7 (89.5 mV dec^{-1}), manifesting accelerated kinetics at the Ni_xS_y-5 interface.

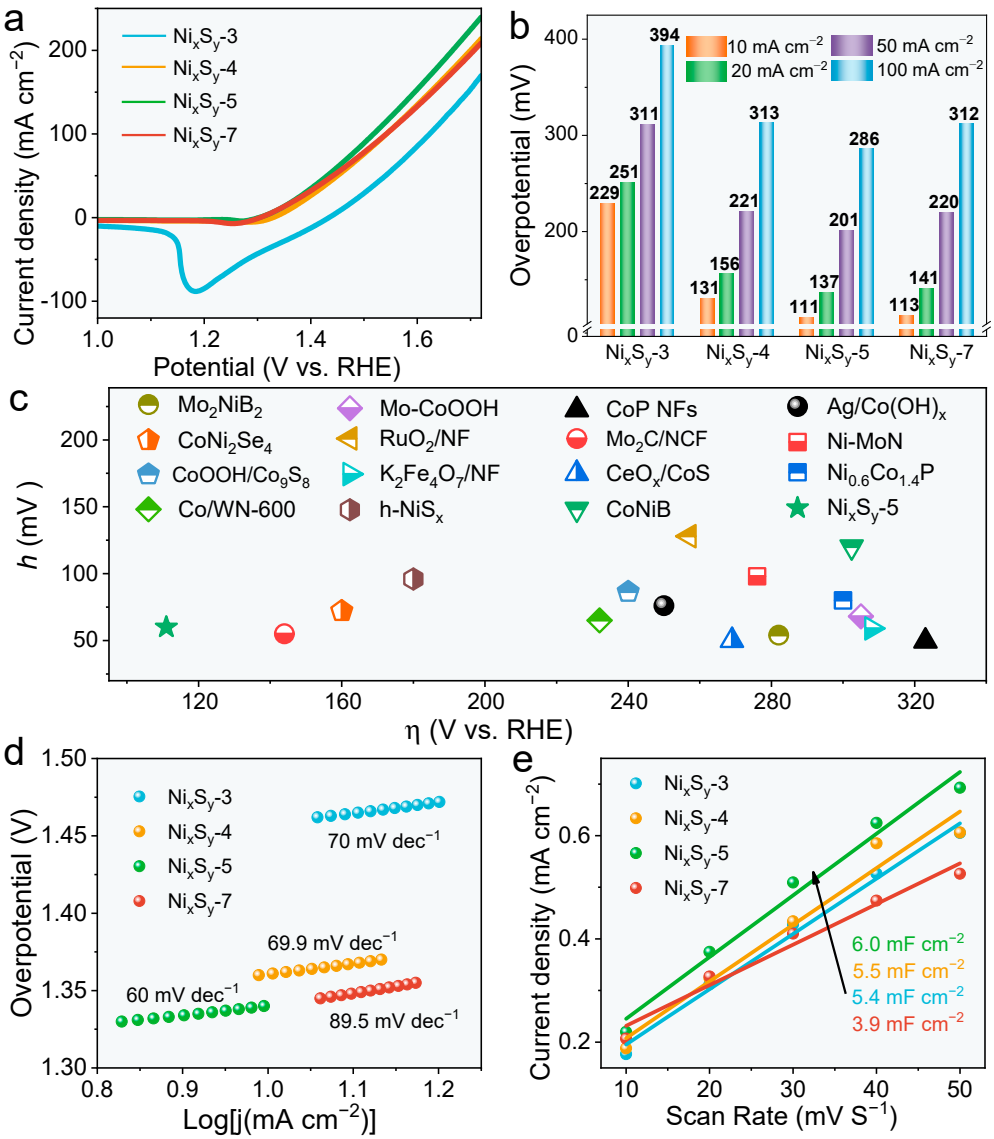

Figure 4. The OER performance data of the as-prepared electrocatalysts in 1.0 M KOH. (**a**) The polarization curves (iR-corrected) measured with a scan rate of 5 mV s^{-1}; (**b**) comparison of the overpotential of as-prepared electrodes at different current densities of 10 mA cm^{-2}, 20 mA cm^{-2}, 50 mA cm^{-2}, and 100 mA cm^{-2}; (**c**) comparison of the overpotential at 10 mA cm^{-2} and the Tafel slope for Ni_xS_y-5 with other recently reported electrocatalysts for OER; (**d**) the corresponding Tafel curves; (**e**) the linear plots of the capacitive current versus the scan rate.

The electrochemical surface areas are probed according to the C_{dl} behaviors for evaluating the catalytic efficiency of the catalysts (Figures 4e and S8). The C_{dl} for Ni_xS_y-7 was 6.0 mF cm^{-2}, which was slightly larger than that of Ni_xS_y-4 and Ni_xS_y-5 (5.4, and 5.5 mF cm^{-2}, respectively), and a considerably increased compared with that of Ni_xS_y-7 at 3.9 mF cm^{-2}. The EIS analysis was carried out to assess the electron transfer kinetics, with semicircles related to the charge transfer resistance (Figure S9), in which the relatively smaller semicircle of Ni_xS_y-5 implies the better charge-transfer kinetics at its electrolyte/electrode interface, thus leading to rapid charge transfer. The OER durability measurements show that the cathode current did not show a noticeable change, indicating its outstanding stability (Figure S10). In summary, Ni_xS_y-5 is obviously a promising

alternative OER non-precious metal electrocatalyst, satisfying the high activity criteria for potential applications in a concentrated alkaline electrolyte, whose activities could rival many those of other non-precious HER electrocatalysts (Figure 4c and Table S2).

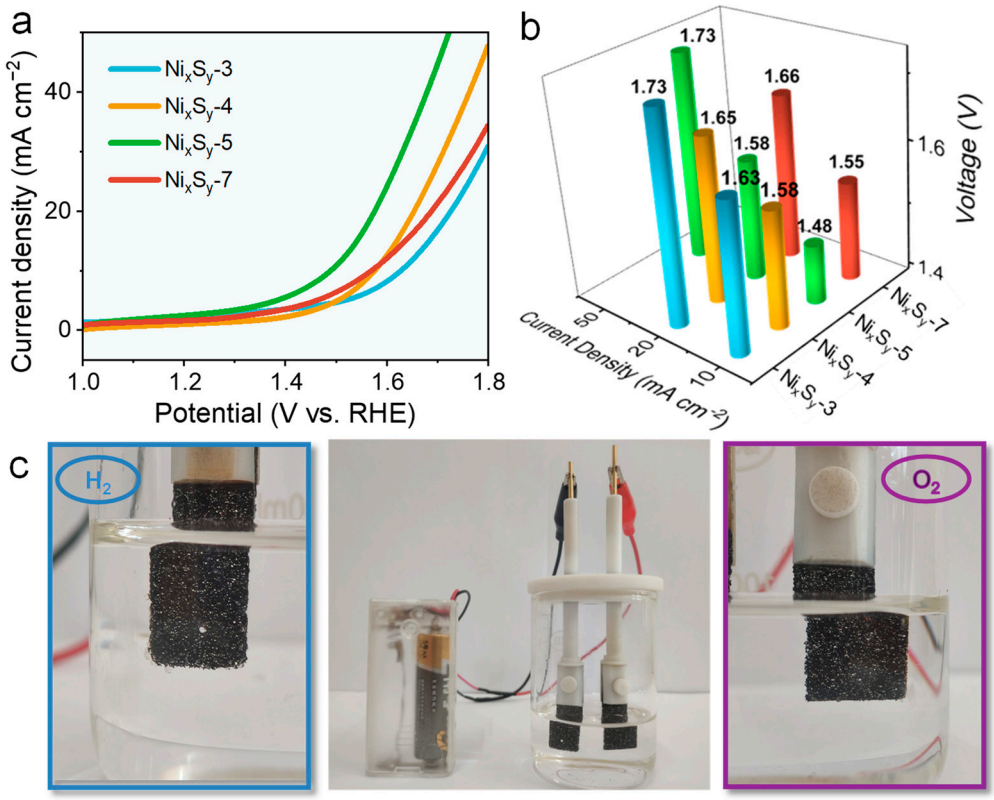

Figure 5. The overall water splitting performance in 1.0 M KOH. (**a**) The polarization curves measured with a scan rate of 5 mV s^{-1}; (**b**) comparison of the overpotential of the as-prepared electrodes at different current densities of 10 mA cm^{-2}, 20 mA cm^{-2}, and 50 mA cm^{-2}; (**c**) a photo image of the H_2 and O_2 generated at the cathode and anode in the Ni_xS_y-5 electrodes.

Considering the superior catalytic activity of the Ni_xS_y-5 electrodes with three-phase components in the OER and HER processes, an overall water splitting electrolyzer was constructed, using Ni_xS_y-5 for both the anode and cathode, under alkaline conditions. For comparison, other catalysts with different phase components were applied as the cathode and anode for overall water splitting in 1 M KOH aqueous solution. The Ni_xS_y-5 catalyst provides a water-splitting current density of 10 mA cm^{-2} at a voltage of only about 1.48 V (Figure 5a), which is obviously superior to the results for the single-phase-component Ni_xS_y-3 electrodes (1.63 V) and the two-phase-component electrodes of Ni_xS_y-4 (1.58 V) and Ni_xS_y-7 (1.55 V). When the current density increased to 50 mA cm^{-2}, the single-phase-component Ni_xS_y-3 electrodes, as well as two-phase component electrodes of Ni_xS_y-4 and Ni_xS_y-7, were unable to continue for overall water splitting, except for the Ni_xS_y-5 electrode with three-phase components (Figure 5b). For more systematically demonstrating the water splitting performances of NixSy-5 electrodes, we have selected three categories for in-depth discussion. First, compared to precious metal-containing electrocatalysts, the cell voltage of 1.48 V is comparable to those of the best-performing precious metal-based electrocatalysts reported to date, such as Ru-NiFe-P/NF (1.47 V) [60], NiFeRu-LDH/NF (1.52 V) [61], and Ru/NiFe LDH-F/NF (1.53 V) [62], and it is obviously superior to those of the majority of precious metal-based electrocatalysts, i.e., $RuTe_2$-400 (1.57 V) [58], Pt/C-RuO_2 (1.67 V) [58], and Ru_2Ni_2 SNs/C (1.58 V) [63]. Second, in the nickel sulfide-based electrocatalysts, the water splitting performances of the NixSy-5 electrodes is surpassed only by several nickel sulfide-based electrocatalysts, such as Mo-NiP_x/NiS_y

(1.42 V) [64] and Mo-Ni_3S_2/Ni_xP_y/NF (1.46 V) [65], and is superior to those of the majority of the corresponding electrocatalysts, i.e., Ni_3S_2@Ni(II)-TC (1.53 V) [9],V-doped Ni_3S_2 (1.55 V) [66], and CoS_8/Ni_3S_2 (1.64 V) [67]. Finally, in the all electrocatalysts, the water splitting performance of the NixSy-5 electrodes is also significantly lower than that of the majority of the state-of-the-art overall-water-splitting electrocatalysts, such as $NiCo_2S_4$ (1.58 V) [68], CoP NFs (1.65 V) [69], and Co_3O_4 NCs (1.91 V) [70]. The durability of the Ni_xS_y-5 electrolyzer was tested in long-term electrolysis experiments at a cell voltage of 1.5 V, and it exhibited a stable cathodic current with almost negligible degradation for at least several hours (Figure S11). More importantly, the electrolyzer could be run by a single-cell 1.5 V AA battery, and numerous gas bubbles were generated on the surface of two Ni_xS_y-5 electrodes, identifying its superior capability for overall water splitting in an alkaline medium (Figure 5c). Since the voltage for overall water splitting is higher than 1.5 V for the single-phase component Ni_xS_y-3 electrodes, as well as for the two-phase component electrodes of Ni_xS_y-4 and Ni_xS_y-7, there is no bubble generation on their surfaces. These results indicate that the Ni_xS_y-5 electrodes could be promising bifunctional electrocatalysts for water splitting because of the special synergistic effect of their three-phase structure (e.g., NiS, Ni_3S_2, and Ni_7S_6), which exhibits the best characteristics both in terms of morphology and internal structure, i.e., uniform rod-like nanoarrays, and the bridged S_2^{2-} ions are more favorable to catalytic activity in the Ni_xS_y-5 electrodes.

4. Conclusions

In summary, by precisely controlling the sulfidation degree in a simple hydrothermal process, we prepared various composition-dependent nickel sulfides from a single-phase component to multiple-phase components (i.e., two-phase components and three-phase components), and further compared the HER and OER performance in a various-phase nickel sulfide-based system. Due to the higher exposed active surface area, the improved charge transfer capacity, and the weaker charge-transfer resistance, the Ni_xS_y-5 nanoarrays with three-phase components showed the remarkable performance of HER and OER, with the overpotentials of 148 and 111 mV, respectively, to deliver the current density of 10 mA cm^{-2}, exceeding that of the majority of non-noble metal HER electrocatalysts. Moreover, Ni_xS_y-5, applied as both the anode and cathode, yields an impressive water-splitting current density of 10 mA cm^{-2} at ≈1.48 V, which is much lower than that of the state-of-the-art overall-water-splitting catalysts (cell voltages > 1.6 V), thus providing a cost-effective alternative for noble metal-based catalysts.

Supplementary Materials: The following supporting information can be downloaded at: https://www.mdpi.com/article/10.3390/coatings13111938/s1, Figure S1: (a–c) The different magnification SEM images of NF surface; Figure S2: SEM images of Ni_xS_y-2 (a), Ni_xS_y-3 (b). The insets exhibit the corresponding high magnification SEM image, respectively; Figure S3: XPS spectra of the survey spectrum for Ni_xS_y-2 (a), Ni_xS_y-3 (b), Ni_xS_y-4 (c), Ni_xS_y-5 (d), Ni_xS_y-6 (e), and Ni_xS_y-7 (f), respectively; Figure S4: XPS spectra of the Ni 2p spectrum for all the as-prepared samples; Figure S5: XPS spectra of the S 2p spectrum for Ni_xS_y-2 (a), Ni_xS_y-3 (b), Ni_xS_y-4 (c), Ni_xS_y-5 (d), Ni_xS_y-6 (e), and Ni_xS_y-7 (f), respectively; Figure S6: XPS spectra of the O 1s spectrum for Ni_xS_y-2 (a), Ni_xS_y-3 (b), Ni_xS_y-4 (c), Ni_xS_y-5 (d), Ni_xS_y-6 (e), and Ni_xS_y-7 (f), respectively; Figure S7: CV curves of the Ni_xS_y-3 (a), Ni_xS_y-4 (b), Ni_xS_y-5 (c), Ni_xS_y-6 (d), respectively, for HER process; Figure S8: CV curves of the Ni_xS_y-3 (a), Ni_xS_y-4 (b), Ni_xS_y-5 (c), Ni_xS_y-6 (d), respectively, for OER process; Figure S9: The corresponding EIS plot for Ni_xS_y-3 electrode, Ni_xS_y-4 electrode, Ni_xS_y-5 electrode, and Ni_xS_y-7 electrode; Figure S10: The stability test toward HER at constant current density of 10 mA cm^{-2} for Ni_xS_y-3 electrode, Ni_xS_y-4 electrode, Ni_xS_y-5 electrode, and Ni_xS_y-7 electrode; Figure S11: Stability test of overall water splitting at constant current density of 10 mA cm^{-2}; Table S1: Summary of the HER activities of recently reported non-noble metal-based electrocatalysts; Table S2: Summary of the OER activities of recently reported non-noble metal-based electrocatalysts; Table S3: Comparison of electrocatalytic performance of Ni_xS_y-5 with recently reported bifunctional electrocatalysts for overall-water-splitting in alkaline media.

Author Contributions: Formal analysis, N.Q. and T.W.; Resources, S.T. and D.W.; Data curation, L.H. and Q.L.; Writing—original draft, N.Q., L.H., T.W., Q.L., S.T., J.G. and D.W.; Supervision, S.T.; Funding acquisition, S.T. All authors have read and agreed to the published version of the manuscript.

Funding: This work was financially supported by the National Natural Science Foundation of China (No. 22278349), the Natural Science Foundation of Hebei Province (No. B2023203026), the Youth Foundation of Hebei Educational Committee (No. QN2020137), the Cultivation Project for Basic Research Innovation of Yanshan University (No. 2021LGZD015), a Subsidy for Hebei Key Laboratory of Applied Chemistry after Operation Performance (No. 22567616H), and the Natural Science Foundation of Heilongjiang Province of China (No. LH2022B025).

Institutional Review Board Statement: Not applicable.

Informed Consent Statement: Not applicable.

Data Availability Statement: Data is contained within the article.

Conflicts of Interest: The authors declare no conflict of interest.

References

1. Montoya, J.H.; Seitz, L.C.; Chakthranont, P.; Vojvodic, A.; Jaramillo, T.F.; Norskov, J.K. Materials for Solar Fuels and Chemicals. *Nat. Mater.* **2016**, *16*, 70–81. [CrossRef]
2. Cook, T.R.; Dogutan, D.K.; Reece, S.Y.; Surendranath, Y.; Teets, T.S.; Nocera, D.G. Solar Energy Supply and Storage for the Legacy and Nonlegacy Worlds. *Chem. Rev.* **2010**, *110*, 6474–6502. [CrossRef] [PubMed]
3. Wang, H.; Lee, H.W.; Deng, Y.; Lu, Z.; Hsu, P.C.; Liu, Y.; Lin, D.; Cui, Y. Bifunctional Non-noble Metal Oxide Nanoparticle Electrocatalysts through Lithium-Induced Conversion for Overall Water Splitting. *Nat. Commun.* **2015**, *6*, 7261. [CrossRef]
4. Li, H.; Zhou, Q.; Liu, F.; Zhang, W.; Tan, Z.; Zhou, H.; Huang, Z.; Jiao, S.; Kuang, Y. Biomimetic Design of Ultrathin Edge-Riched FeOOH@Carbon Nanotubes as High-Efficiency Electrocatalysts for Water Splitting. *Appl. Catal. B* **2019**, *255*, 117755. [CrossRef]
5. Shang, X.; Tang, J.-H.; Dong, B.; Sun, Y. Recent Advances of Nonprecious and Bifunctional Electrocatalysts for Overall Water Splitting. *Sustainable Energ. Fuels* **2020**, *4*, 3211–3228. [CrossRef]
6. You, B.; Sun, Y. Innovative Strategies for Electrocatalytic Water Splitting. *Acc Chem. Res.* **2018**, *51*, 1571–1580. [CrossRef] [PubMed]
7. Pan, Y.; Sun, K.; Liu, S.; Cao, X.; Wu, K.; Cheong, W.C.; Chen, Z.; Wang, Y.; Li, Y.; Liu, Y.; et al. Core-Shell ZIF-8@ZIF-67-Derived CoP Nanoparticle-Embedded N-Doped Carbon Nanotube Hollow Polyhedron for Efficient Overall Water Splitting. *J. Am. Chem. Soc.* **2018**, *140*, 2610–2618. [CrossRef]
8. Parkinson, G.S.; Novotny, Z.; Jacobson, P.; Schmid, M.; Diebold, U. Room Temperature Water Splitting at the Surface of Magnetite. *J. Am. Chem. Soc.* **2011**, *133*, 12650–12655. [CrossRef]
9. Zhang, F.; Zhao, R.; Wang, Y.; Han, L.; Gu, J.; Niu, Z.; Yuan, Y.; Qu, N.; Meng, J.; Wang, D. Superwettable Surface-Dependent Efficiently Electrocatalytic Water Splitting based on Their Excellent Liquid Adsorption and Gas Desorption. *Chem. Eng. J.* **2023**, *452*, 139513. [CrossRef]
10. Roger, I.; Shipman, M.A.; Symes, M.D. Earth-Abundant Catalysts for Electrochemical and Photoelectrochemical Water Splitting. *Nat. Rev. Chem.* **2017**, *1*, 3. [CrossRef]
11. Kibsgaard, J.; Chorkendorff, I. Considerations for the Scaling-up of Water Splitting Catalysts. *Nat. Energy* **2019**, *4*, 430–433. [CrossRef]
12. Mahmood, N.; Yao, Y.; Zhang, J.W.; Pan, L.; Zhang, X.; Zou, J.J. Electrocatalysts for Hydrogen Evolution in Alkaline Electrolytes: Mechanisms, Challenges, and Prospective Solutions. *Adv. Sci.* **2018**, *5*, 1700464. [CrossRef] [PubMed]
13. Zheng, Y.; Jiao, Y.; Vasileff, A.; Qiao, S.Z. The Hydrogen Evolution Reaction in Alkaline Solution: From Theory, Single Crystal Models, to Practical Electrocatalysts. *Angew. Chem. Int. Ed.* **2018**, *57*, 7568–7579. [CrossRef] [PubMed]
14. Levinas, R.; Tsyntsaru, N.; Cesiulis, H.; Viter, R.; Grundsteins, K.; Loreta, T.T.; Norkus, E. Electrochemical Synthesis of a WO_3/MoS_x Heterostructured Bifunctional Catalyst for Efficient Overall Water Splitting. *Coatings* **2023**, *13*, 673. [CrossRef]
15. Wu, Y.; Li, G.-D.; Liu, Y.; Yang, L.; Lian, X.; Asefa, T.; Zou, X. Overall Water Splitting Catalyzed Efficiently by an Ultrathin Nanosheet-Built, Hollow Ni_3S_2-Based Electrocatalyst. *Adv. Funct. Mater.* **2016**, *26*, 4839–4847. [CrossRef]
16. Jin, H.; Wang, J.; Su, D.; Wei, Z.; Pang, Z.; Wang, Y. In Situ Cobalt-Cobalt Oxide/N-Doped Carbon Hybrids as Superior Bifunctional Electrocatalysts for Hydrogen and Oxygen Evolution. *J. Am. Chem. Soc.* **2015**, *137*, 2688–2694. [CrossRef]
17. Ren, J.; Antonietti, M.; Fellinger, T.-P. Efficient Water Splitting Using a Simple Ni/N/C Paper Electrocatalyst. *Adv. Energy Mater.* **2015**, *5*, 1401660. [CrossRef]
18. Yang, Y.; Fei, H.; Ruan, G.; Tour, J.M. Porous Cobalt-based Thin Film as a Bifunctional Catalyst for Hydrogen Generation and Oxygen Generation. *Adv. Mater.* **2015**, *27*, 3175–3180. [CrossRef]
19. Jiang, N.; You, B.; Sheng, M.; Sun, Y. Electrodeposited Cobalt-Phosphorous-Derived Films as Competent Bifunctional Catalysts for Overall Water Splitting. *Angew. Chem. Int. Ed.* **2015**, *54*, 6251–6254. [CrossRef]
20. Stern, L.-A.; Feng, L.; Song, F.; Hu, X. Ni_2P as a Janus catalyst for Water Splitting: The Oxygen Evolution Activity of Ni_2P Nanoparticles. *Energy Environ. Sci.* **2015**, *8*, 2347–2351. [CrossRef]

21. Zhang, G.; Wang, G.; Liu, Y.; Liu, H.; Qu, J.; Li, J. Highly Active and Stable Catalysts of Phytic Acid-Derivative Transition Metal Phosphides for Full Water Splitting. *J. Am. Chem. Soc.* **2016**, *138*, 14686–14693. [CrossRef] [PubMed]
22. Guo, Y.; Tong, Y.; Chen, P.; Xu, K.; Zhao, J.; Lin, Y.; Chu, W.; Peng, Z.; Wu, C.; Xie, Y. Engineering the Electronic State of a Perovskite Electrocatalyst for Synergistically Enhanced Oxygen Evolution Reaction. *Adv. Mater.* **2015**, *27*, 5989–5994. [CrossRef] [PubMed]
23. Lu, X.; Yim, W.L.; Suryanto, B.H.; Zhao, C. Electrocatalytic Oxygen Evolution at Surface-Oxidized Multiwall Carbon Nanotubes. *J. Am. Chem. Soc.* **2015**, *137*, 2901–2907. [CrossRef]
24. Wang, F.; Li, J.; Wang, F.; Shifa, T.A.; Cheng, Z.; Wang, Z.; Xu, K.; Zhan, X.; Wang, Q.; Huang, Y.; et al. Enhanced Electrochemical H_2 Evolution by Few-Layered Metallic $WS_{2(1-x)}Se_{2x}$ Nanoribbons. *Adv. Funct. Mater.* **2015**, *25*, 6077–6083. [CrossRef]
25. Pfrommer, J.; Lublow, M.; Azarpira, A.; Gobel, C.; Lucke, M.; Steigert, A.; Pogrzeba, M.; Menezes, P.W.; Fischer, A.; Schedel-Niedrig, T.; et al. A Molecular Approach to Self-Supported Cobalt-Substituted ZnO Materials as Remarkably Stable Electrocatalysts for Water Oxidation. *Angew. Chem. Int. Ed.* **2014**, *53*, 5183–5187. [CrossRef] [PubMed]
26. Yin, T.H.; Liu, B.J.; Lin, Y.W.; Li, Y.S.; Lai, C.E.; Lan, Y.P.; Choi, C.; Chang, H.C.; Choi, Y.M. Electrodeposition of Copper Oxides as Cost-Effective Heterojunction Photoelectrode Materials for Solar Water Splitting. *Coatings* **2022**, *12*, 1839. [CrossRef]
27. Giovanni, D.C.; Wang, W.-A.; Nowak, S.; Grenèche, J.-M.; Lecoq, H.; Mouton, L.; Giraud, M.; Tard, C. Bioinspired Iron Sulfide Nanoparticles for Cheap and Long-Lived Electrocatalytic Molecular Hydrogen Evolution in Neutral Water. *ACS Catal.* **2014**, *4*, 681–687. [CrossRef]
28. Feng, L.L.; Yu, G.; Wu, Y.; Li, G.D.; Li, H.; Sun, Y.; Asefa, T.; Chen, W.; Zou, X. High-Index Faceted Ni_3S_2 Nanosheet Arrays as Highly Active and Ultrastable Electrocatalysts for Water Splitting. *J. Am. Chem. Soc.* **2015**, *137*, 14023–14026. [CrossRef]
29. Kong, D.; Wang, H.; Lu, Z.; Cui, Y. $CoSe_2$ Nanoparticles Grown on Carbon Fiber Paper: An Efficient and Stable Electrocatalyst for Hydrogen Evolution Reaction. *J. Am. Chem. Soc.* **2014**, *136*, 4897–4900. [CrossRef]
30. Popczun, E.J.; McKone, J.R.; Read, C.G.; Biacchi, A.J.; Wiltrout, A.M.; Lewis, N.S.; Schaak, R.E. Nanostructured Nickel Phosphide as an Electrocatalyst for the Hydrogen Evolution Reaction. *J. Am. Chem. Soc.* **2013**, *135*, 9267–9270. [CrossRef]
31. Liu, Q.; Tian, J.; Cui, W.; Jiang, P.; Cheng, N.; Asiri, A.M.; Sun, X. Carbon Nanotubes Decorated with CoP Nanocrystals: A Highly Active Non-Noble-Metal Nanohybrid Electrocatalyst for Hydrogen Evolution. *Angew. Chem. Int. Ed.* **2014**, *53*, 6710–6714. [CrossRef]
32. Perevoznikov, S.S.; Yakovlev, I.V.; Tsybulskaya, L.S.; Lapina, O.B. Synthesis and Composition Study of Electrochemically Deposited Ni-P Coating with Increased Surface Area. *Coatings* **2021**, *11*, 1071. [CrossRef]
33. Li, L.; Wang, X.; Guo, Y.; Li, J. Synthesis of an Ultrafine CoP Nanocrystal/Graphene Sandwiched Structure for Efficient Overall Water Splitting. *Langmuir* **2020**, *36*, 1916–1922. [CrossRef]
34. Han, X.; Yu, C.; Zhou, S.; Zhao, C.; Huang, H.; Yang, J.; Liu, Z.; Zhao, J.; Qiu, J. Ultrasensitive Iron-Triggered Nanosized Fe-CoOOH Integrated with Graphene for Highly Efficient Oxygen Evolution. *Adv. Energy Mater.* **2017**, *7*, 1602148. [CrossRef]
35. Chen, P.; Zhou, T.; Zhang, M.; Tong, Y.; Zhong, C.; Zhang, N.; Zhang, L.; Wu, C.; Xie, Y. 3D Nitrogen-Anion-Decorated Nickel Sulfides for Highly Efficient Overall Water Splitting. *Adv. Mater.* **2017**, *29*, 1701584. [CrossRef] [PubMed]
36. Hao, J.; Yang, W.; Hou, J.; Mao, B.; Huang, Z.; Shi, W. Nitrogen Doped NiS_2 Nanoarrays with Enhanced Electrocatalytic Activity for Water Oxidation. *J. Mater. Chem. A* **2017**, *5*, 17811–17816. [CrossRef]
37. Yu, X.Y.; Yu, L.; Wu, H.B.; Lou, X.W. Formation of Nickel Sulfide Nanoframes from Metal-Organic Frameworks with Enhanced Pseudocapacitive and Electrocatalytic Properties. *Angew. Chem. Int. Ed.* **2015**, *54*, 5331–5335. [CrossRef] [PubMed]
38. Jiang, N.; Tang, Q.; Sheng, M.; You, B.; Jiang, D.; Sun, Y. Nickel Sulfides for Electrocatalytic Hydrogen Evolution under Alkaline Conditions: A Case study of Crystalline NiS, NiS_2, and Ni_3S_2 Nanoparticles. *Catal. Sci. Technol.* **2016**, *6*, 1077–1084. [CrossRef]
39. Qu, Y.; Yang, M.; Chai, J.; Tang, Z.; Shao, M.; Kwok, C.T.; Yang, M.; Wang, Z.; Chua, D.; Wang, S.; et al. Facile Synthesis of Vanadium-Doped Ni_3S_2 Nanowire Arrays as Active Electrocatalyst for Hydrogen Evolution Reaction. *ACS Appl. Mater. Interfaces* **2017**, *9*, 5959–5967. [CrossRef]
40. Cheng, N.; Liu, Q.; Asiri, A.M.; Xing, W.; Sun, X. A Fe-Doped Ni_3S_2 Particle Film as a High-Efficiency Robust Oxygen Evolution Electrode with Very High Current Density. *J. Mater. Chem. A* **2015**, *3*, 23207–23212. [CrossRef]
41. Liu, Q.; Xie, L.; Liu, Z.; Du, G.; Asiri, A.M.; Sun, X. A Zn-Doped Ni_3S_2 Nanosheet Array as a High-Performance Electrochemical Water Oxidation Catalyst in Alkaline Solution. *Chem. Commun.* **2017**, *53*, 12446–12449. [CrossRef] [PubMed]
42. Cui, Z.; Ge, Y.; Chu, H.; Baines, R.; Dong, P.; Tang, J.; Yang, Y.; Ajayan, P.M.; Ye, M.; Shen, J. Controlled Synthesis of Mo-Doped Ni3S2 Nano-rods: An Efficient and Stable Electro-catalyst for Water Splitting. *J. Mater. Chem. A* **2017**, *5*, 1595–1602. [CrossRef]
43. Zykov, F.; Selyanin, I.; Shishkin, R.; Kartashov, V.; Borodianskiy, K.; Yuferov, Y. Study of the Photocatalytic Properties of Ni-Doped Nanotubular Titanium Oxide. *Coatings* **2023**, *13*, 144. [CrossRef]
44. Wen, L.; Xu, R.; Mi, Y.; Lei, Y. Multiple Nanostructures based on Anodized Aluminium Oxide Templates. *Nat. Nanotechnol.* **2017**, *12*, 244–250. [CrossRef] [PubMed]
45. Cui, R.; Gu, J.; Wang, N.; Wang, Y.; Huang, X.; Zhang, S.; Lu, L.; Wang, D. Organic Dye Molecule Intercalated Vanadium Oxygen Hydrate Enables High-Performance Aqueous Zinc-Ion Storage. *Small* **2023**, 2307849. [CrossRef] [PubMed]
46. Petriev, I.; Pushankina, P.; Glazkova, Y.; Andreev, G.; Baryshev, M. Investigation of the Dependence of Electrocatalytic Activity of Copper and Palladium Nanoparticles on Morphology and Shape Formation. *Coatings* **2023**, *13*, 621. [CrossRef]

47. Li, H.; Wu, X.; Wang, P.; Song, S.; He, M.; Li, C.; Wang, W.; Fang, Z.; Yuan, X.; Song, W.; et al. Interface Engineering of Hollow CoO/Co_4S_3@CoO/Co_4S_3 Heterojunction for Highly Stable and Efficient Electrocatalytic Overall Water Splitting. *ACS Sustain. Chem. Eng.* **2022**, *10*, 13112–13124. [CrossRef]
48. He, W.; Liu, H.; Cheng, J.; Li, Y.; Liu, C.; Chen, C.; Zhao, J.; Xin, H.L. Modulating the Electronic Structure of Nickel Sulfide Electrocatalysts by Chlorine Doping toward Highly Efficient Alkaline Hydrogen Evolution. *ACS Appl. Mater. Interfaces* **2022**, *14*, 6869–6875. [CrossRef] [PubMed]
49. Raj, D.; Scaglione, F.; Fiore, G.; Rizzi, P. Cost-Effective Nanoporous Gold Obtained by Dealloying Metastable Precursor, Au33Fe67, Reveals Excellent Methanol Electro-Oxidation Performance. *Coatings* **2022**, *12*, 831. [CrossRef]
50. Wang, L.; Zhang, L.; Ma, W.; Wan, H.; Zhang, X.; Zhang, X.; Jiang, S.; Zheng, J.Y.; Zhou, Z. In Situ Anchoring Massive Isolated Pt Atoms at Cationic Vacancies of α-$Ni_xFe_{1-x}(OH)_2$ to Regulate the Electronic Structure for Overall Water Splitting. *Adv. Funct. Mater.* **2022**, *32*, 2203342. [CrossRef]
51. Vrubel, H.; Merki, D.; Hu, X. Hydrogen evolution catalyzed by MoS_3 and MoS_2 particles. *Energy Environ. Sci.* **2012**, *5*, 6136–6144. [CrossRef]
52. Cai, Z.; Zhang, Y.; Zhao, Y.; Wu, Y.; Xu, W.; Wen, X.; Zhong, Y.; Zhang, Y.; Liu, W.; Wang, H.; et al. Selectivity Regulation of CO_2 Electroreduction through Contact Interface Engineering on Superwetting Cu Nanoarray Electrodes. *Nano Res.* **2018**, *12*, 345–349. [CrossRef]
53. Weber, T.; Muijsers, J.C.; Wolput, J.H.M.C.; Verhagen, C.P.J.; Niemantsverdriet, J.W. Basic Reaction Steps in the Sulfidation of Crystalline MoO_3 to MoS_2, As Studied by X-ray Photoelectron and Infrared Emission Spectroscopy. *J. Phys. Chem.* **1996**, *100*, 14144–14150. [CrossRef]
54. Yin, J.; Li, Y.; Lv, F.; Lu, M.; Sun, K.; Wang, W.; Wang, L.; Cheng, F.; Li, Y.; Xi, P.; et al. Oxygen Vacancies Dominated NiS_2/CoS_2 Interface Porous Nanowires for Portable Zn-Air Batteries Driven Water Splitting Devices. *Adv. Mater.* **2017**, *29*, 1704681. [CrossRef] [PubMed]
55. Poolwong, J.; Del Gobbo, S.; D'Elia, V. Transesterification of Dimethyl Carbonate with Glycerol by Perovskite-Based Mixed Metal Oxide Nanoparticles for the Atom-Efficient Production of Glycerol Carbonate. *J. Ind. Eng. Chem.* **2021**, *104*, 43–60. [CrossRef]
56. Del Gobbo, S.; Poolwong, J.; Valerio D'Elia, V.; Ogawa, M. Simultaneous Controlled Seeded-Growth and Doping of ZnO Nanorods with Aluminum and Cerium: Feasibility Assessment and Effect on Photocatalytic Activity. *Cryst. Growth Des.* **2020**, *20*, 5508–5525. [CrossRef]
57. Kessaratikoon, T.; Saengsaen, S.; Del Gobbo, S.; D'Elia, V.; Sooknoi, T. High Surface Area ZnO-Nanorods Catalyze the Clean Thermal Methane Oxidation to CO_2. *Catalysts* **2022**, *12*, 1533. [CrossRef]
58. Liu, Y.; Wang, L.; Li, D.; Wang, K. State-of-Health Estimation of Lithium-Ion Batteries based on Electrochemical Impedance Spectroscopy: A Review. *Prot. Contr. Mod. Pow.* **2023**, *8*, 41. [CrossRef]
59. Qu, M.; Jiang, Y.; Yang, M.; Liu, S.; Guo, Q.; Shen, W.; Li, M.; He, R. Regulating electron density of NiFe-P nanosheets electrocatalysts by a trifle of Ru for high-efficient overall water splitting. *Appl. Catal. B Environ.* **2020**, *263*, 118324. [CrossRef]
60. Chen, G.; Wang, T.; Zhang, J.; Liu, P.; Sun, H.; Zhuang, X.; Chen, M.; Feng, X. Accelerated Hydrogen Evolution Kinetics on NiFe-Layered Double Hydroxide Electrocatalysts by Tailoring Water Dissociation Active Sites. *Adv. Mater.* **2018**, *30*, 1706279. [CrossRef]
61. Wang, Y.; Zheng, P.; Li, M.; Li, Y.; Zhang, X.; Chen, J.; Fang, X.; Liu, Y.; Yuan, X.; Dai, X.; et al. Interfacial Synergy between Dispersed Ru Sub-nanoclusters and Porous NiFe Layered Double Hydroxide on Accelerated Overall Water Splitting by Intermediate Modulation. *Nanoscale* **2020**, *12*, 9669–9679. [CrossRef] [PubMed]
62. Tang, B.; Yang, X.; Kang, Z.; Feng, L. Crystallized $RuTe_2$ as Unexpected Bifunctional Catalyst for Overall Water Splitting. *Appl. Catal. B Environ.* **2020**, *278*, 119281. [CrossRef]
63. Ding, J.B.; Shao, Q.; Feng, Y.G.; Huang, X.Q. Ruthenium-Nickel Sandwiched Nanoplates for Efficient Water Splitting Electrocatalysis. *Nano Energy* **2018**, *47*, 1–7. [CrossRef]
64. Wang, J.; Zhang, M.; Yang, G.; Song, W.; Zhong, W.; Wang, X.; Wang, M.; Sun, T.; Tang, Y. Heterogeneous Bimetallic Mo-NiP_x/NiS_y as a Highly Efficient Electrocatalyst for Robust Overall Water Splitting. *Adv. Funct. Mater.* **2021**, *16*, 2101532. [CrossRef]
65. Luo, X.; Ji, P.; Wang, P.; Cheng, R.; Chen, D.; Lin, C.; Zhang, J.; He, J.; Shi, Z.; Li, N.; et al. Interface Engineering of Hierarchical Branched Mo-Doped Ni_3S_2/Ni_xP_y Hollow Heterostructure Nanorods for Efficient Overall Water Splitting. *Adv. Energy. Mater.* **2020**, *10*, 1903891. [CrossRef]
66. Zheng, X.; Zhang, Y.; Liu, H.; Fu, D.; Chen, J.; Wang, J.; Zhong, C.; Deng, Y.; Han, X.; Hu, W. In Situ Fabrication of Heterostructure on Nickel Foam with Tuned Composition for Enhancing Water-Splitting Performance. *Small* **2018**, *14*, e1803666. [CrossRef]
67. Du, F.; Shi, L.; Zhang, Y.; Li, T.; Wang, J.; Wen, G.; Alsaedi, A.; Hayat, T.; Zhou, Y.; Zou, Z. Foam–Like Co_9S_8/Ni_3S_2 Heterostructure Nanowire Arrays for Efficient Bifunctional Overall Water–Splitting. *Appl. Catal. B Environ.* **2019**, *253*, 246–252. [CrossRef]
68. Kang, Z.; Guo, H.; Wu, J.; Sun, X.; Zhang, Z.; Liao, Q.; Zhang, S.; Si, H.; Wu, P.; Wang, L.; et al. Engineering an Earth-Abundant Element-Based Bifunctional Electrocatalyst for Highly Efficient and Durable Overall Water Splitting. *Adv. Funct. Mater.* **2019**, *29*, 1807031. [CrossRef]

69. Ji, L.; Wang, J.; Teng, X.; Meyer, T.J.; Chen, Z. CoP Nanoframes as Bifunctional Electrocatalysts for Efficient Overall Water Splitting. *ACS Catal.* **2019**, *10*, 412–419. [CrossRef]
70. Du, S.; Ren, Z.; Zhang, J.; Wu, J.; Xi, W.; Zhu, J.; Fu, H. Co_3O_4 Nanocrystal Ink Printed on Carbon Fiber Paper as a Large-Area Electrode for Electrochemical Water Splitting. *Chem. Commun.* **2015**, *51*, 8066–8069. [CrossRef]